

# Influence of Aggregated Powder Structures on Sintering Behaviour of Multilayer Hydroxyapatite Laminates

E. Hahn<sup>\*1</sup>, J. Hum<sup>1</sup>, J. Will<sup>1</sup>, K. Zuo<sup>2</sup>, D. Jiang<sup>2</sup> and P. Greil<sup>1</sup>

<sup>1</sup>University of Erlangen-Nuremberg, Department of Materials Science (Glass and Ceramics) Martensstr. 5, D-91058 Erlangen, Germany

<sup>2</sup>Shanghai Institute of Ceramics, Chinese Academy of Sciences, The State Key Lab of High Performance Ceramics and Superfine Structures, 1295 Ding-Xi Rd, Shanghai 200050, China

received September 2, 2010; received in revised form October 20, 2010; accepted October 21, 2010

## Abstract

Aqueous tape-cast slurries of hydroxyapatite with a solid loading of 32 vol% were prepared from various fractions of aggregated (mean particle size 4.7 – 5.6 µm) and dispersed powder (mean particle size 0.17 – 0.29 µm). Multilayer laminates were prepared and the shrinkage and density of the laminates sintered at 1250 °C were measured. While fractional density in the green laminates remains almost constant at 0.52, a pronounced increase in fractional sintered density from 0.96 to > 0.99 was observed with decreasing fraction of aggregated powder. Residual pore size and pore number density were reduced from 0.58 µm to 0.48 µm and 0.049 pores/µm<sup>2</sup> to 0.019 pores/µm<sup>2</sup>, respectively. The multilayer laminates attained a mean bending strength of 118 ± 10 MPa measured with the bi-axial bending test. An osteosynthesis plate design was fabricated for demonstration of the potential of sintered multilayer laminates.

*Keywords:* Hydroxyapatite, laminate sintering, aggregated and dispersed powder

## I. Introduction

Hydroxyapatite (Ca<sub>10</sub>(PO<sub>4</sub>)<sub>6</sub>(OH)<sub>2</sub>, HA) ceramics are of considerable interest for clinical applications owing to the similarity of their crystal structure and chemistry to the inorganic mineral phase of bone and teeth<sup>1, 2</sup>. Porous and dense HA are widely used as orthopaedic and dental implant materials as they elicit a favourable biological response and form a bond with the surrounding tissue<sup>3</sup>. Dense HA is described as having a maximum microporosity of < 5 vol% with the micropores measuring < 1 µm in diameter and a crystallite size exceeding 200 nm<sup>4</sup>. Depending on the manufacturing technique, the composition and the residual porosity, however, HA suffers from high brittleness ( $K_{Ic} \leq 1 \text{ MPam}^{1/2}$ ) as well as low mechanical properties that may scatter in a wide range and have hindered the widespread use of HA implants in long-term load-bearing applications<sup>5, 6</sup>. While dense stoichiometric HA may attain a high Young's modulus of approx. 130 GPa derived from atomistic *ab initio* calculations and 147 ± 10 GPa measured by nanoindentation<sup>7</sup>, increasing porosity and pore size owing to incomplete densification upon sintering reduce the values significantly to 35 – 103 GPa<sup>8</sup>. Furthermore, compressive strength and flexural strength were reported to vary in a wide range from 200 – 900 MPa and 17 – 110 MPa, respectively<sup>6, 8</sup>. Although strengthening and toughening concepts have been applied, such as dispersion of ductile particles (Ag), alumina platelets, zirconia particles, or carbon nanotubes

and fibres, to form HA composites with higher toughness<sup>9–13</sup>, it is desirable to minimize the porosity and size of pores to improve the mechanical properties of HA implants<sup>14, 15</sup>.

Fabrication procedures for dense HA ceramics are quite diversified, including sintering and hot pressing of gel-derived or hydrothermally precipitated, spray-dried and calcined powders with particle sizes in the submicron to nanoscale range<sup>16, 17</sup>. Major problems of sintering HA arise from the thermal decomposition above a critical temperature (which limits sintering temperature) and formation of secondary phases that may undergo further decomposition or hydrolysis reactions. Aggregation of submicron crystallite powders during drying and calcination can cause non-uniformity in the packing of particles in a green compact, and thus prevent full densification during sintering<sup>18</sup>. To avoid retardation of densification during pressureless sintering, the Ca/P molar ratio has to be very near to the stoichiometric ratio of 1.67<sup>19</sup>. Stoichiometric HA was found to remain stable in dry or moist air up to 1200 °C<sup>20, 21</sup>. At temperatures in the range 1350 – 1500 °C, however, HA becomes unstable and decomposes to α-tricalcium phosphate (Ca<sub>3</sub>(PO<sub>4</sub>)<sub>2</sub>), tetracalcium phosphate (Ca<sub>4</sub>(PO<sub>4</sub>)O) and calcium pyrophosphate (Ca<sub>2</sub>P<sub>2</sub>O<sub>7</sub>)<sup>22</sup>. Moreover, it has been reported that CaO may form during sintering when the Ca/P molar ratio exceeds the stoichiometric composition (> 1.67)<sup>21</sup>. Volume changes associated with the hydrolysis reaction (CaO + H<sub>2</sub>O → Ca(OH)<sub>2</sub>, ΔV/V<sub>CaO</sub> = + 101 %) and carbonate formation (Ca(OH)<sub>2</sub> + CO<sub>2</sub> → CaCO<sub>3</sub>, ΔV/V<sub>Ca(OH)2</sub> = + 11 %)

\* Corresponding author: Eike.Hahn@ww.uni-erlangen.de

when exposed to H<sub>2</sub>O and CO<sub>2</sub> respectively, may generate residual stresses and induce microcrack formation, which reduces the modulus of rupture<sup>5,21,23,24</sup>. If the Ca/P molar ratio of HA is lower than 1.67, β- or α-tricalcium phosphate (TCP) may form<sup>25</sup>, giving rise to enhanced slow crack growth susceptibility and biodegradability of the HA ceramics. Thus, a high density of HA requires careful control of the HA composition, reduction of the sintering temperatures below the critical decomposition threshold and eventually external pressure to promote rapid densification (hot-pressing).

Reduction of the sintering temperature may be achieved by applying HA powders with submicron or even nanoscale particle size<sup>26,27</sup>. Powders with particle diameters smaller than 1 μm, however, tend to form aggregate domains due to dominance of surface forces (van der Waals) over gravity, which upon heat treatment may form aggregated particles<sup>28</sup>. During heating, non-uniform sintering may occur, which is likely to obstruct sintering. Differential stresses caused by local variation of the packing structure in a mixture of aggregate and dispersed powder tend to become higher when the ratio of densification to creep relaxation increases as is the case with decreasing particle size<sup>29</sup>. Furthermore, analyses of differential sintering phenomena in inhomogeneous powder compacts have shown that, with decreasing particle size, stresses generated at density transitions, e.g. interfaces between aggregated and dispersed packing regions, may give rise to redistribution of porosity and even attain critical values to cause microstructure defect formation (flaws, cracks)<sup>29–31</sup>. Thus, even single-phase and stoichiometric HA powders were reported to achieve only densities which did not exceed 93 % – 98 % upon pressureless sintering<sup>28, 32, 33</sup>.

The aim of this study was to investigate the influence of aggregated powder structures on the sintering of multilayer HA laminates. Layered and thin-walled HA ceramics derived from tape-cast and extrusion processing are becoming interesting for fabrication of HA implants with optimized structure design such as pore gradient structures and multilayer composites<sup>34–36</sup> or microchannelled ceramics<sup>37</sup>. Thus, there is an incentive to develop HA films with controlled porosity<sup>38</sup> as well as multilayer laminates with high fractional density by pressureless sintering. Bimodal HA powders containing different fractions of a pre-calcined aggregated powder in a matrix of dispersed submicron powder were prepared. Tapes were manufactured by doctor-blade casting and laminated by cold compression (30 °C) to form multilayer stacks. No external pressure was applied and the sintering temperature was limited to 1250 °C to avoid thermal decomposition of the HA. Residual porosity, density, and modulus of rupture were characterized and discussed in respect of the powder size distribution ratios.

## II. Experimental Procedures

### (1) Powder processing

Bimodal HA slurries were prepared by combining different fractions of agglomerated HA and of dispersed nanoscale HA. The aggregated powder (denoted C

(coarse)) was obtained by calcination of the as-received HA powder (Hydroxyapatite for bioceramics, Merck KGaG, Darmstadt, D, specific surface area of 68.6 m<sup>2</sup>/g, Ca/P molar ratio of 1.67) at 900 °C for 2 h. After calcination a mean particle size of approximately 3.9 μm was measured by means of laser granulometry (Master Sizer 2000, APA 2000 with Hydro 2000S; Malvern Instruments, Worcestershire, GB) and the specific surface area analysed with the BET method (N<sub>2</sub> adsorption, ASAP 2000, Micromeritics, Norcross, USA) was reduced to 11.2 m<sup>2</sup>/g. The fine powder (denoted F) was prepared by milling the calcined HA powder in an attritor mill filled with zirconia balls (diameter ~ 100 – 200 μm). A milling time of 3 h proved long enough to ensure disintegration of the weakly granulated HA powder and to yield a submicron HA powder with an almost monomodal particle size distribution.

Tape-casting slurries containing different fractions of C and F powders were mixed and homogenized in one processing step for 24 h in a shaker mixer (Turbula, W.A. Bachhofen, Basel, CH). A typical tape-casting slurry was composed of 58 wt% (32 vol%) HA powder, 21.8 wt% PVA-based binder/plasticizer (Dulacol B4014, Zschimmer und Schwarz, Lahnstein, D, 55 wt% active binder in aqueous solution), 2 wt% dispersant (NH<sub>4</sub>-Polycarboxylate, Melpers 3440, BASF, Trostberg, D), and distilled water. Grain size distributions were measured after mixing (Master Sizer 2000, APA 2000 with Hydro 2000S; Malvern Instruments, Worcestershire, GB). A fine-to-coarse powder size ratio λ<sub>F</sub> was determined by integration of the two monomodal grain size distribution functions H<sub>C</sub>(G) and H<sub>F</sub>(G) of the coarse (aggregated) and of the fine HA powder fractions, respectively, according to

$$\lambda_F = \frac{\int_{0.01}^{0.7} H_F(G) dG}{\int_{0.01}^{0.7} H_F(G) + \int_{0.7}^{100} H_C(G) dG} \quad (1)$$

The experimentally measured distributions in the two separate size ranges  $G < 0.7 \mu\text{m}$  and  $G > 0.7 \mu\text{m}$  were fitted to a log normal distribution (Origin 7.5, OriginLab Corp. Northampton, USA)

$$H_{C,F}(G) = y_0 + \frac{A}{Gs\sqrt{2\pi}} \exp \left[ -\frac{\left( \ln \frac{G}{G_{50}} \right)^2}{2s^2} \right] \quad (2)$$

where  $y_0$ ,  $A$ , and  $s$  are the offset, the normalizing factor and the standard deviation, respectively. The fraction of coarse (aggregated) powder is given as  $\lambda_C = 1 - \lambda_F$ .

### (2) Tape casting, lamination and sintering

Tapes were prepared with a double-chamber doctor blade casting head on silicon-coated PET support foil. The casting speed was 700 mm/min and the distance between the blade and the casting head was adjusted to 200 μm, resulting in a mean thickness of the cast tapes of approximately 100 μm (i.e. shrinkage of tape in thickness reaches

50 %). The cast slurries were dried at room temperature and subsequently laminated in a lamination press (Polystat 200 t, Servitec Maschinenbau GmbH, Wustermark, D) by applying a pressure of 40 MPa for 15 minutes. Rectangular samples measuring  $40 \times 40 \times 1.7 \text{ mm}^3$  were manufactured from stacks composed of 22 tape layers (e.g. shrinkage upon laminate pressing approx. 23 %). No additional adhesive was applied to the tapes prior to lamination pressing. The thermoplastic binder present in the tape was selected for its low glass transition temperature of  $-20^\circ\text{C}$  to allow cold lamination bonding at  $30^\circ\text{C}$ . This technique is based on gluing the adjacent tapes by means of an adhesive film at room temperature under a low pressure<sup>39</sup>. A single-step thermal annealing process was applied which included binder burnout and sintering of the ceramic laminate. Up to  $600^\circ\text{C}$  a heating rate of 1 K/min was applied to allow organic binder, deflocculant and adhesive burnout. Above  $600^\circ\text{C}$  a heating and cooling rate of 3.6 K/min was applied. The multilayer laminate specimens were sintered in air atmosphere at  $1250^\circ\text{C}$ , for 2 h. The dimensional change during sintering was measured by dilatometry (Dil 402 C, Netzsch, Selb, D). The samples ( $12 \text{ mm} \times 6 \text{ mm} \times 1.7 \text{ mm}$ ) were cut from HA laminates ( $\lambda_F = 0.97$  and  $\lambda_P = 0.1$ ). The linear shrinkage caused by sintering of the longest dimension of the sample was detected using a connecting rod dilatometer. The rod and the substrate supporting the sample consisted of  $\text{Al}_2\text{O}_3$ . The shrinkage data was corrected for the thermal expansion of  $\text{Al}_2\text{O}_3$ . Up to  $600^\circ\text{C}$  a heating rate of 1 K/min was applied. Above  $600^\circ\text{C}$  up to  $1250^\circ\text{C}$  with a dwell time of 2 h a heating rate of 3.6 K/min was applied.

### (3) Characterization

The particle morphology of the HA powders was analysed with SEM (Quanta 200, FEI, Eindhoven, NL). Ca and P contents before and after calcination were determined by means of ICP analysis (Spectro Fleming Modula, Spectro Analytical Instruments, Kleve, D). The crystalline phase composition (HA - JCPDS 009-0432,  $\beta$ -TCP - JCPDS 009-0169) was determined with XRD (Kristalloflex D500, Siemens, Karlsruhe, D) using monochromated Cu-K $\alpha$  radiation ( $\lambda_{\text{Cu}} = 0.1542 \text{ nm}$ ). The crystallite size  $G_{\text{cry}}$  was determined by means of the Scherrer equation ( $G_{\text{cry}} \approx 0.94 \lambda_{\text{Cu}} / (w \cos\theta)$ ). The full width at half maxima  $w$  was determined from the prominent peaks (002) and (211) of HA. The temperature-dependent phase composition of the ceramic tapes was determined with HT-XRD (XRD, Siemens, D 500 equipped with an Anton Paar HTK 10 chamber, D). Powder from debinded ( $600^\circ\text{C}$ ) ceramics tapes consisting of dispersed nanoscale HA was analysed by means of HT-XRD to cover the influence of processing on the temperature-dependent phase composition of HA. XRD spectra were measured at  $1150^\circ\text{C}$ ,  $1200^\circ\text{C}$ ,  $1250^\circ\text{C}$ ,  $1300^\circ\text{C}$  and  $1350^\circ\text{C}$ , after 1 h dwell time. Length, width, height, and mass of green specimens were measured for density calculation. The sintered density was measured with the Archimedes method. The microstructure of HA laminate cross-sections perpendicular to the laminate stacking was analysed with SEM. Prior to examination the specimen surface was sputtered with gold.

The modulus of rupture of the multilayered HA ceramics was measured by means of biaxial bending using a ring-on-ring test<sup>40</sup> (Instron 4204, Instron Corp., Canton, MA, USA). Measurements were performed with load and support rings of 8.2 mm and 18 mm in diameter, respectively, and a cross-head velocity of 0.5 mm/min. Samples were used as sintered without grinding and polishing. Fracture stress  $\sigma_f$  was derived from the specimen geometry, the loading geometry and the load applied  $F_{\text{max}}$  according to<sup>40</sup>

$$\sigma_f = \frac{3F_{\text{max}}}{2\pi h^2} \left( (1-\nu) \frac{r_2^2 - r_1^2}{2(e(1+\sqrt{2})/4)} + (1+\nu) \ln \frac{r_2}{r_1} \right) \quad (3)$$

where  $\nu$  is the Poisson ratio ( $\nu = 0.25$ ),  $r_1$  is the radius of the load-ring ( $r_1 = 4.1 \text{ mm}$ ),  $r_2$  is the radius of the support ring ( $r_2 = 9 \text{ mm}$ ),  $e$  is the edge length of the quadratic samples ( $e \approx 31 \text{ mm}$ ), and  $h$  is the sample height ( $h \approx 1.4 \text{ mm}$ ). Compared to uniaxial four-point or three-point bending testing, the biaxial concentric ring test is simpler to perform because the maximum stressed surface area is confined within the central region of the disc specimen and effects of edge preparation are minimized.

## III. Results and Discussion

### (1) Powder composition and tape density

Chemical analysis confirmed a stoichiometric Ca/P ratio of 1.672 measured in the as-received HA powder which remained unchanged upon calcination at  $900^\circ\text{C}$  for 2 h. Fig. 1 shows SEM micrographs of the as-received and of the calcined HA powder, respectively. The aggregates in the as-received HA powder consist of crystallites of a mean size  $G_{\text{cry}} \approx 28 \text{ nm}$  as calculated from the specific surface area  $S_V \approx 68.6 \text{ m}^2/\text{g}$  and the density  $\rho = 3.156 \text{ g/cm}^3$  ( $G_{\text{cry}} \approx 6/(S_V \rho)$ ). From XRD line broadening a crystallite size of  $G_{\text{cry}} \approx 34 \text{ nm}$  was derived. Laser granulometry of both HA powders resulted in a mean aggregate size ( $G_{\text{agg}}$ ) of approximately  $3.9 \mu\text{m}$ , indicating that the mean aggregate size remained almost unaffected by the calcination treatment. In contrast, coarsening of the crystallites resulted in a pronounced increase of the crystallite size after calcination ( $150 \text{ nm}$  (specific surface area) and  $80 \text{ nm}$  (XRD)).

Stoichiometric HA with a Ca/P ratio of 1.67 was reported to remain stable during heat treatment up to  $1200^\circ\text{C}$ <sup>41</sup>. HT-XRD (not shown) reveals HA as the only crystalline phase present up to  $1250^\circ\text{C}$ . The average heating rate during HT-XRD measurement was approximately 0.6 K/min. At  $1300^\circ\text{C}$  traces of  $\alpha$ -TCP were detected indicating that the decomposition reaction of HA to TCP ( $\text{Ca}_{10}(\text{PO}_4)_3/(\text{OH})_2 \rightarrow \text{Ca}_3(\text{PO}_4)_2 + \text{CaO} + \text{H}_2\text{O}$ ) commences between  $1250 - 1300^\circ\text{C}$ <sup>42</sup>. In order to prevent formation of decomposition phases, the sintering temperature of the laminate ceramics was therefore limited to a maximum temperature of  $1250^\circ\text{C}$ . Furthermore, previous examinations of the grain growth behaviour of HA have shown a moderate grain growth rate at this temperature which accelerated significantly at higher temperatures<sup>43</sup>, resulting in a decrease in toughness and strength<sup>4</sup>.

Fig. 2 shows the grain size distributions of the five slurries prepared for tape casting measured with laser granu-

lometry. Two distinct grain size maxima may be separated as expected from mixing of the fine and coarse fractions. From the areas under the  $H_{C,F}(G)$  curves the fraction of fine powder  $\lambda_F$  was derived according to Eq. (1) for each powder mixture:  $\lambda_F \approx 0.52, 0.56, 0.57, 0.72, \text{ and } 0.97$ .

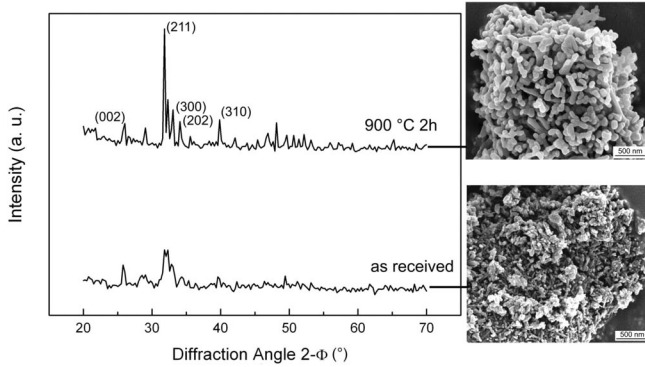


Fig. 1: XRD diffraction spectra and SEM micrographs of HA as received and calcined at 900 °C 2 h.

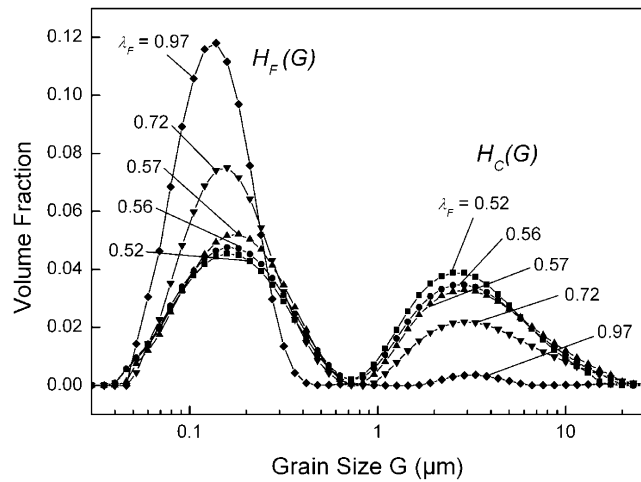


Fig. 2: Grain size distributions of slurries containing differing contents of agglomerates.  $H_C(G)$ , and  $H_F(G)$  denote the separate distributions of the coarse (aggregated) and the fine (dispersed) powder fractions with  $\lambda_F = 0.52, 0.56, 0.57, 0.72, \text{ and } 0.97$ .

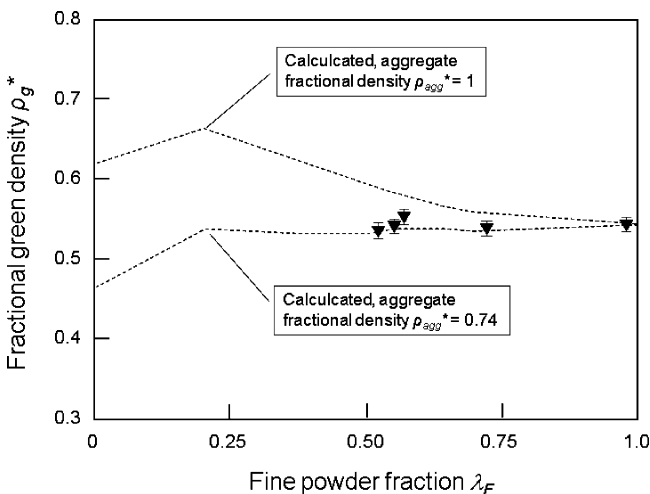


Fig. 3: Green densities of multilayer laminates produced from powders with different  $\lambda_F$ . The calculated curves were derived from Eq. (4) using the experimentally measured grain size distributions from Fig. 2.

Both separate distributions may well be fitted to log normal distributions (Table 1). The mean particle size,  $G_{50}$ , derived from distribution analyses ranges from 4.7 - 5.6  $\mu\text{m}$  for the coarse powder fraction  $H_C(G)$  and from 0.17 - 0.29  $\mu\text{m}$  for the fine powder fraction  $H_F(G)$ . While powder  $\lambda_F = 0.52$  is bimodal with approximately equal coarse and fine powder fractions,  $\lambda_F = 0.97$  equals an almost monomodal powder size distribution.

Table 1: Grain size distributions of tape cast slurries prepared from powder mixtures with various fine grain fractions  $\lambda_F$  measured by means of laser granulometry.

$\lambda_F$	0.52	0.56	0.57	0.72	0.97
<b>Fine fraction</b>					
$G_{50}$	0.279	0.289	0.286	0.211	0.168
s	0.733	0.750	0.713	0.552	0.502
$y_0$	-0.651	-0.776	-0.909	-0.222	-1.077
A	2.055	2.299	2.446	1.955	2.430
<b>Coarse fraction</b>					
$G_{50}$	4.722	5.128	5.672	5.526	4.730
s	0.701	0.720	0.742	0.712	0.486
$y_0$	-0.101	-0.024	-0.051	-0.039	-0.061
A	26.173	25.255	26.970	16.547	0.957

Fig. 3 shows the green density of the HA multilayer laminates as a function of the powder particle size ratio  $\lambda_F$ . The green density remains almost independent of the variation of  $\lambda_F$  at a constant level of approximately 0.52. From the principles of bimodal mixtures of spheres one should expect a maximum packing density (filling of small interstitial pores) at a coarse/fine particle volume fraction of approximately 0.23 which decreases almost linearly with increasing fraction of fine particles<sup>44</sup>. It was found that the packing density increases as the size ratio increases to  $\sim 15$ , but is relatively unchanged at higher size ratios. Since the aggregates of the coarse powder fraction  $H_C(G)$  are not dense particles, but exhibit even a lower fractional density of 0.41 compared to 0.52 in the fine-grained powder fraction, it is clear that density in the green laminates should not decrease but remain constant or even increase slightly with increasing  $\lambda_F$  from 0.52 to 0.97. The expected density as a function of  $\lambda_F$  was calculated according to the fractal-like concept of Funk and Dinger<sup>45</sup>

$$\frac{CPFT}{100} = \frac{G^n - G_S^n}{G_L^n - G_S^n} \quad (4)$$

where  $CPFT$  is the cumulative percent finer than  $G$ ,  $G$  is the measured particle size,  $G_L$  is the largest particle diameter,  $G_S$  is the smallest particle diameter, and  $n$  is the distribution modulus (0.37). The fractional density  $\rho^*$  (e.g. packing density) is obtained from the cumulative volume fraction finer than  $G$  ( $CVFT$ ) ( $\rho^* = 1 - CVFT$  at  $G_S$  (100)). The fractional densities calculated from Eq. (4) are shown

as the dashed lines in Fig. 3. For the case of the coarse particles to be fully dense e.g. the fractional particle density  $\rho_{agg}^* = 1$ , a maximum in fractional density is calculated from the measured particle size distributions to occur at a fine particle fraction  $\lambda_F \sim 0.2$  which decreases with increasing  $\lambda_F$ , (Fig. 3). In contrast, the experimental densities measured on the green specimens were found not to change significantly with increasing  $\lambda_F$ . Taking into account that the aggregate particles are porous (Fig. 1), the measured values of packing density are well reproduced by the calculated curve for  $\rho_{agg}^* \sim 0.74$  (the fractional packing density of the aggregate particles,  $\rho_{agg}^*$ , was estimated from  $\rho_{agg}^* \approx 1 - (\rho_{id}^* - \rho_{gr}^*)$  where  $\rho_{id}^*$  is the calculated ( $\rho_{id}^* \sim 0.8$ ) (assuming dense particles) and  $\rho_{gr}^*$  is the measured fractional green density ( $\rho_{gr}^* \sim 0.54$ ) of the powder fraction  $\lambda_F = 0$ , respectively).

(2) Sintering

Fig. 4 shows the sintering strain and sintering strain rate of specimens with the grain size distribution functions  $\lambda_F = 0.52$  and  $\lambda_F = 0.97$ . Accelerated sintering shrinkage started at approximately 950 °C with a distinct maximum of shrinkage rate at 1200 – 1250 °C. The bimodal heterogeneous powder microstructure ( $\lambda_F = 0.52$ ) shows a slight shift of the strain rate curve to higher temperatures ( $\Delta T \approx 20 - 45$  °C) and a reduction of the maximum value by 13.7 % compared to the homogeneous fine powder sample ( $\lambda_F = 0.97$ ). Accordingly, a higher total sintering strain of 19 % ( $\lambda_F = 0.97$ ) compared to 16 % ( $\lambda_F = 0.52$ ) was observed, which resulted in a sintered density of 0.99 compared to 0.96, respectively.

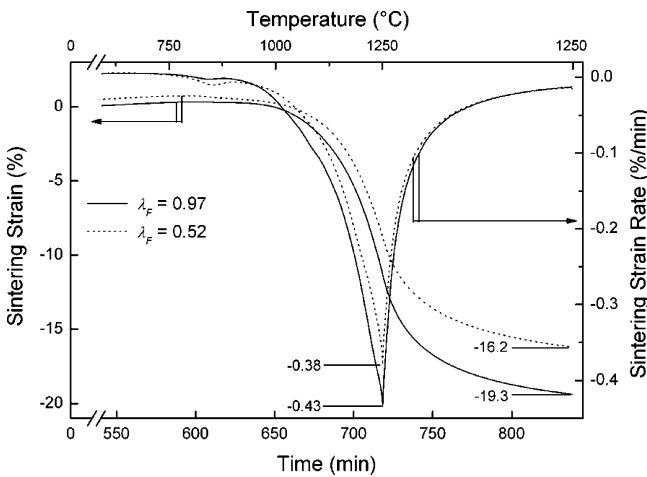


Fig. 4: Sintering strain and sintering strain rate of HA laminate prepared from powders with the lowest  $\lambda_F = 0.52$  and the highest  $\lambda_F = 0.97$  fine powder fraction.

Experimental observations have shown that the final density of sintered ceramic composite depends strongly on the initial packing density of the powder matrix<sup>46</sup>. In particular, density fluctuations were recognized as one of the major problems in achieving a high sintered density<sup>47</sup>. Following analysis of the sintering behaviour of bimodal powder compacts derived by Raj and Bordia<sup>29</sup>, the total change in density of a sphere (aggregate) – matrix composite,  $\Delta\rho_0$ , with both regions sintered, but at different rates, can be expressed by

$$\overline{\Delta\rho_0} = \left[ 1 - \exp(-k\bar{t}) \right] + (1 - \lambda_F) \left[ 1 + k' \frac{p_0^F}{p_0^C} \right] \left[ \exp(k\bar{t}) - \exp\left(-\frac{\bar{t}}{r}\right) \right] \quad (5)$$

where  $\bar{t}$  is the time normalized with respect to the time constant for densification ( $\bar{t} = t/\tau_a$  with  $t$  the time and  $\tau_a$  the time required to reach 64 % of the difference between the theoretical and the green density), and  $p_0^F$  and  $p_0^C$  are the sintering stresses in the fine and the coarse powder packing regions, respectively. The variables  $k$  and  $k'$  express the ratio of the creep rate to the densification rate in the fine powder fraction and in the coarse powder aggregates (based on constitutive laws, expressions for  $k$  and  $k'$  were derived for viscous sintering<sup>31,48</sup>). The variable  $r$  denotes the ratio of the sintering rate in the fast sintering region to the sintering rate of the slow sintering region and may characterize the density fluctuations in the green powder microstructure (e.g. “heterogeneity”). The normalized density change is defined as

$$\overline{\Delta\rho_0} = \frac{\rho(t) - \rho_g}{\rho_{th} - \rho_g} \quad (6)$$

where  $\rho(t)$  is the time-dependent density,  $\rho_g$  is the green density and  $\rho_{th}$  the density of the dense HA ( $\rho_{th} = 3.156$  g/cm<sup>3</sup>). If  $k, k' \rightarrow \infty$ , instantaneous relaxation reduces the incompatibility stresses to zero and Eq. (5) equals the simple rule of mixture which defines an upper bound for densification

$$\overline{\Delta\rho_0} = \lambda_F \left[ 1 - \exp(-\bar{t}) \right] + (1 - \lambda_F) \left[ 1 - \exp\left(-\frac{\bar{t}}{r}\right) \right] \quad (7)$$

Similarly, models referring to the effects of transient back stresses generally predict a linear relation between the volume fraction of inclusion and retardation of sintering rate of the composite compared to that of the inclusion-free matrix<sup>30,48-50</sup>. Since the difference in fractional density between the aggregate fraction (0.74) and the dispersed matrix fraction (0.52) is relatively small, the rule of mixture should apply to the HA multilayer laminate sintering at least to a first approximation.

Fig. 5 shows the experimentally measured sintered density and the values calculated according to Eq. (7) (taking  $\rho_g^* = 0.52$ ,  $\rho_{th} = 3.156$  g/cm<sup>3</sup>,  $\bar{t} = 4$  and  $r = 2$ ). In contrast to the green density (Fig. 3), the sintered density of HA multilayer laminates increased almost linearly with increasing  $\lambda_F$  and reached a maximum value of 0.99 for  $\lambda_F = 0.97$ . Though the model discussed above does not account for the specific rate-controlling densification mechanisms of HA, the calculated curve reproduces well the effect of increasing powder packing heterogeneity caused by the aggregated coarse powder fraction, i.e. decreasing  $\lambda_F$ . As a consequence, powder processing of HA should aim to generate a homogeneous powder packing structure in order to attain a dense microstructure by means of pressureless sintering.

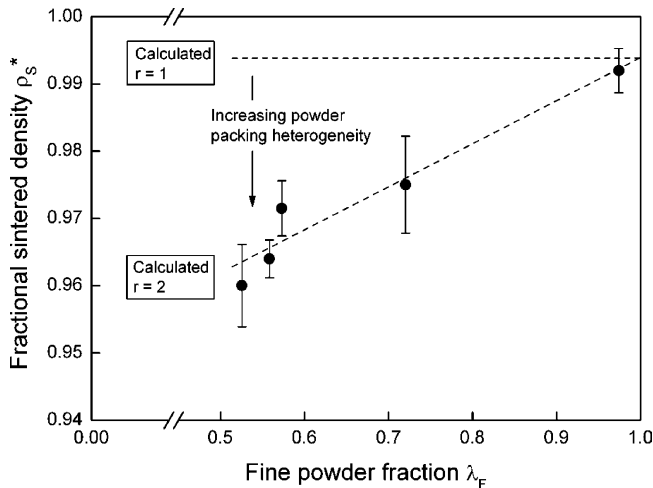


Fig. 5: Fractional sintered densities of the multilayer HA laminates prepared from different powders. For comparison, fractional densities were estimated according to Eq. (7) for the case of uniform ( $r=1$ ) and non-uniform ( $r=2$ ) sintering of the coarse and fine powder fractions, respectively.

### (3) Microstructure and strength

Fig. 6 shows a laminate cross-section perpendicular to the laminate stacking ( $\lambda_F=0.97$ ). The mean thickness of the cast tapes is approximately 100  $\mu\text{m}$ . Subtracting a sintering shrinkage of 18 %, at least two interphases should be apparent in the micrograph (Fig. 6). No microstructural inhomogeneity marking interphases between two HA layers can be detected, indicating an excellent consolidation of the HA tapes. Fig. 7 shows laminate cross-sections perpendicular to the laminate stacking of specimens with the grain size ratio values  $\lambda_F=0.52$  and 0.97. In dense HA ceramics the grain size and the remnant microporosity strongly influence the mechanical properties both in compression and in tension. The crystallite size of the sintered specimen ( $\lambda_F=0.97$ ) was measured from SEM micrographs of fracture surfaces (Table 2). Only moderate growth of the crystallite size was observed during sintering at 1250  $^{\circ}\text{C}$  ranging from 1.85 ( $\lambda_F=0.52$ ) to 1.19  $\mu\text{m}$  ( $\lambda_F=0.97$ ). Exaggerated grain growth with grain sizes exceeding 10  $\mu\text{m}$  were analyzed in HA sintered at temperatures  $\geq 1350$   $^{\circ}\text{C}$  with the grain size increasing exponentially with the sintering temperature <sup>43</sup>.

The mean pore size and pore density (number of pores per area) were determined by means of optical analysis of micrographs taken from cross-sections perpendicular to the interfaces. It was found that the mean pore diameter decreased from 0.58  $\mu\text{m}$  to 0.48  $\mu\text{m}$  with  $\lambda_F$  increasing from 0.52 to 0.97. Simultaneously, the mean areal pore density decreased from  $49 \times 10^3$  (pores/ $\text{mm}^2$ ) to  $19 \times 10^3$  (pores/ $\text{mm}^2$ ), which corresponds to a reduction of mean pore distance from 4.5  $\mu\text{m}$  to 7.3  $\mu\text{m}$ , respectively.

Fracture strength values of sintered and hot-pressed single phase HA ceramics reported in the literature vary in a wide range from 80 – 120 MPa <sup>4,6</sup>. Remnant porosity due to incomplete densification, microstructure defects from processing as well as thermal decomposition of HA are commonly considered to cause reduced strength as well as a low Weibull modulus, i.e. enhanced scattering. Mechanisms underlying temperature-strength interrelations for

dense (> 95 % dense, pores closed) HA were investigated by comparative assessment of temperature effects on tensile strength, Weibull modulus, apparent density, decomposition <sup>51</sup>. Significant dehydroxylation occurred above  $\sim 800$   $^{\circ}\text{C}$ . Strength peaked at  $\sim 80$  MPa just before the attainment of closed porosity ( $\sim 95$  % dense). For higher temperatures (closed porosity), the strength dropped sharply to  $\sim 60$  MPa due to the closure of dehydroxylation pathways, and then stabilized at  $\sim 60$  MPa. At very high temperatures (> 1350  $^{\circ}\text{C}$ ), the strength dropped catastrophically to  $\sim 10$  MPa, corresponding to the decomposition of HA to tricalcium phosphate and the associated sudden release of the remaining bonded water.

Table 2: Microstructural variables of prepared HA specimens.

$\lambda_F$	0.52	0.56	0.57	0.72	0.97
Mean grain size ( $\mu\text{m}$ )	1.85	1.73	1.74	1.47	1.19
Fractional density	0.518	0.522	0.534	0.518	0.522
Mean pore size ( $\mu\text{m}$ )	0.64	0.51	0.47	0.42	0.43
Areal pore density ( $1/\text{mm}^2$ )	$103 \times 10^3$	$142 \times 10^3$	$131 \times 10^3$	$112 \times 10^3$	$57 \times 10^3$
Mean pore distance [ $\mu\text{m}$ ]	3.1	2.6	2.8	2.9	4.2

The uniform microstructure and low residual porosity in the sintered HA multilayer laminate specimens give rise to enhanced mechanical properties. A mean biaxial bending strength of  $118 \pm 10$  MPa was measured for the HA specimen. Significantly lower biaxial bending values of failure stresses of  $24 \pm 5$  MPa were reported from single-phase HA isostatically pressed and sintered at 1250  $^{\circ}\text{C}$  <sup>52</sup>. Although the amount of reduction of failure stress in the concentric ring test compared to four-point-loading test is dependent on the failure statistics (i.e. Weibull), previous results indicated that the concentric ring test provides a conservative value (for sintered  $\text{Al}_2\text{O}_3$  the biaxial strength was measured approx. 8 – 9 % lower than in uniaxial four point bending testing <sup>53</sup>).

Multilayer HA ceramics with improved mechanical behaviour might become more interesting for replacement of metal implants in low or mild loading situations for short- and long-term support in bone regeneration. Major advantages are seen in the accelerated formation of a bone-bonding interface, no necessity for a second operation to remove the implant, and no visualization difficulties in monitoring tissue regeneration with magnetic resonance imaging. In order to demonstrate the sintering capability of the multilayer laminate ceramics prepared from HA powder ( $\lambda_F=0.97$ ) an osteosynthesis plate design (56 mm  $\times$  19.8 mm  $\times$  1.25 mm) for fracture stabilization was manufactured. Diamond machining of the plate containing one row of four holes for screws (hole diameter 4.5 mm) was accomplished by diamond cutting and

drilling of the green laminate. Owing to the excellent laminate bonding strength, no interface delamination damaging occurred during machining and sintering. Thus, multilayer laminate processing offers high potential for transfer to laminated object manufacturing (LOM rapid prototyping), which may offer great flexibility for manufacturing of customized designs and of multiphase calcium phosphate ceramics with graded structure<sup>36</sup>.

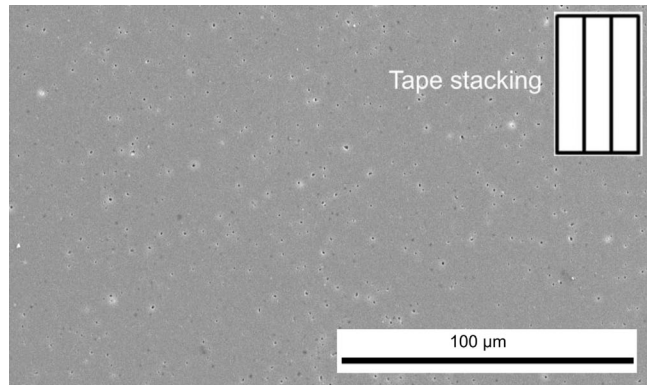


Fig. 6: Cross-section covering two layer interphases of HA laminate sintered at 1250 °C for 2 h.

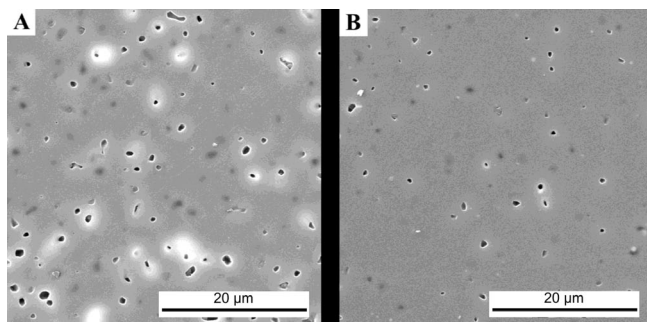


Fig. 7: SEM micrographs of HA laminate sintered at 1250 °C for 2 h: (A)  $\lambda_F = 0.52$  and (B)  $\lambda_F = 0.97$ .

#### IV. Conclusions

Hydroxyapatite multilayer laminates were processed by means of aqueous tape casting and pressureless sintering. With decreasing fraction of aggregated HA powder differential sintering in the non-uniform powder microstructure decreases and densification is promoted. HA powders with a stoichiometric molar Ca/P ratio and a monomodal submicron particle size distribution were demonstrated to achieve fractional densities >99 % at a sintering temperature of 1250 °C. Owing to smaller pore sizes and lower pore number in the sintered microstructure a maximum bidirectional bending strength of 118 MPa was reached. Multilayer lamination processing offers great flexibility in implant design and may be applied in rapid prototyping techniques.

#### Acknowledgements

The authors gratefully acknowledge the financial support from the German Research Foundation (GR 961/28-1).

#### References

- de Groot, K., Klein, C.P.A.T., Wolke, J.G.C., de Blik-Hogervorst, J.M.A.: CRC Handbook of Bioactive Calcium Phosphates, CRC Boca Raton, FL, 2, 3, (1990). 3.
- Dorozhkin, S.V.: Calcium orthophosphates in Nature, Biology and Medicine, Materials, 2, 399-498, (2009).
- Hench, L.L.: Bioceramics, *J. Amer. Ceram. Soc.*, **81**, 1705-1728, (1998).
- LeGeros, R.Z., LeGeros, J.P.: Dense Hydroxyapatite, in An Introduction to Bioceramics, editors L.L. Hench, J. Wilson, World Scientific Publ., Singapore, 139-180, (1999).
- Jarcho, M., Bolen, C. H., Thomas, M. B., Bobick, J., Kay, J. F., Doremus, R. H.: Hydroxylapatite Synthesis and Characterization in Dense Form, *J. Mater. Res.*, **11** [11], 2027-2035, (1976).
- de With, G., van Dijk, H. J. A., Hattu, N., Prijs, K.: Preparation, Microstructure and Mechanical Properties of Dense Polycrystalline Hydroxyapatite, *J. Mater. Sci.*, **16** [6], 1592-1598, (1981).
- Snyders, R., Music, D., Sigumonrong, D., Schlenberger, B., Jensen, J., Schneider, J.M.: Experimental and *ab initio* study of the mechanical properties of hydroxyapatite, *Appl. Phys. Lett.*, **90**, 193902, (2007).
- Jarcho, M.: Calcium phosphate ceramics as hard tissue prosthetics, *Clin. Orthop.*, **157**, 259-278, (1981).
- Zhang, X., Gubbels, G.H.M., Terpstra, R.A., Metselaar, R.: Toughening of Calcium Hydroxyapatite with Silver Particles, *J. Mat. Sci.* **32**, 235-243, (1997).
- Gautier, S., Champion, E., Bernache-Assollant, D.: Toughening characterization in alumina platelet-hydroxyapatite matrix composites, *J. Mat. Sci. Mat. Med.* **10**, 533-540, (1999).
- Cioni, B., Lazzeri, A., Gallone, G., Levita, G.: Synthesis of Bioactive Hydroxyapatite-Zirconia Toughened Composites for Bone Replacement, in *Adv. Sci. Techn.* **57**, Trans Tech Publ. CH, 31-36, (2008).
- White, A.A., Best, S., Kinloch, I.A.: Hydroxyapatite – Carbon Nanotube Composites for Biomedical Applications: A Review, *Int. J. Appl. Ceram. Techn.*, **4**, 1-13 (2007).
- Dorner-Reisel, A., Müller, E., Tomandl, G.: Short Fiber-Reinforced Hydroxyapatite-Bioceramics, *Adv. Eng. Mat.*, **6**, 572-577, (2004).
- Fanovich, M. A., Porto Lopez, J.M.: Influence of temperature and additives on the microstructure and sintering behavior of hydroxyapatites with different Ca/P ratios, *J. Mat. Sci. Mat. Med.*, **9**, 53-60, (1998).
- Wang, P.E., Chaki, T.K.: Sintering behaviour and mechanical properties of hydroxyapatite and dicalcium phosphate, *J. Mat. Sci. Mat. Med.*, **4**, 150-158, (1993).
- Layrolle, P., Ito, A., Tateishi, T.: Sol-Gel Synthesis of Amorphous Calcium Phosphate Sintering into Microporous Hydroxyapatite Bioceramics, *J. Amer. Ceram. Soc.*, **81**, 1421-1428, (1998).
- Ahn, E.S., Gleason, N.J., Nakahira, A., Ying, J.Y.: Nanostructure Processing of Hydroxyapatite Bioceramics, *Nanoletters*, **1**, 149-153, (2001).
- Majiling, J., Znaik, P., Palova, A., Svetik, S., Kovalik, S., Agrawal, D.K., Roy, R.: Sintering of the Ultrahigh Pressure Densified Hydroxyapatite Monolithic Xerogels, *J. Mat. Res.*, **12**, 198-202, (1997).
- van Landuyt, P., Li, F., Keustermans, J.P., Streydio, J.M., Delannay, E.: The influence of high sintering temperature on the mechanical properties of hydroxyapatite, *J. Mat. Sci. Mat. Med.*, **6**, 8-13, (1995).
- Zhou, J., Zhang, X., Chen, J., Zeng, S., de Groot, K.: High-temperature characteristic of synthetic hydroxyapatite, *J. Mat. Sci. Mat. Med.*, **4**, 83-85, (1993).

- 21 Suchanek, W., Yoshimura, M.: Processing and properties of hydroxyapatite-based bio-materials for use as hard tissue replacement implants, *J.Mater.Res.*, **13**, 94-117, (1998).
- 22 Wang, C.K., Ju, C.P., Chern Lin, J.H.: Effect of doped bioactive glass on structure and properties of sintered hydroxyapatite, *Mat.Chem.Phys.*, **53**, 138-149, (1998).
- 23 Ruys, A.J., Brandwood, A., Milthorpe, B.K., Dickson, M.R., Zeigler, K.A., Sorrell, C.C.: The effects of sintering atmosphere on the chemical compatibility of hydroxylapatite and particulate additives at 1200 °C, *J. Mat. Sci. Mat. Med.*, **6**, 297-301, (1995).
- 24 Kijima, T., Tsutsumi, M.: Preparation and thermal properties of dense polycrystalline oxyhydroxyapatite, *J.Amer.Ceram.Soc.*, **62**, 455-460, (1979).
- 25 Han, Y., Xu, K., Lu, J., Wu, Z.: The structural characteristics and mechanical behaviors of non-stoichiometric apatite coatings sintered in air atmosphere, *J. Biomed. Mater. Res.*, **45**, 198-203, (1999).
- 26 Groza, J.R., Dowding, R.J.: Nanoparticulate Materials Densification, *Nan.St.Mat.*, **7**, 749-768, (1996).
- 27 Gibson, I.R., Ke, S., Best, S.M., Bonfield, W.: Effect of powder characteristics on the sinterability of hydroxyapatite powders, *J.Mat.Sci.Mat.Med.*, **12**, 163-171, (2001).
- 28 Dynys, F.W., Halloran, J.W.: Influence of Aggregates on Sintering, *J.Amer.Ceram.Soc.*, **67**, 596-601, (1984).
- 29 Raj, R., Bordia, R.: Sintering Behaviour of Bi-Modal Powder Compacts, *Acta Metall.*, **32**, 1003-1019, (1984).
- 30 Evans, A.G.: Considerations of Inhomogeneity Effects in Sintering, *J.Amer.Ceram.Soc.*, **65**, 497-501, (1982).
- 31 Scherrer, G.W.: Viscous Sintering of a Bimodal Pore-Size Distribution, *J.Amer.Ceram.Soc.*, **67**, 709-715, (1984).
- 32 de With, G., van Dijk, H. J. A., Hattu, N., Prijs, K.: Preparation, microstructure and mechanical properties of dense polycrystalline hydroxyapatite, *J.Mat.Sci.*, **16**, 1592-1598, (1981).
- 33 Kalita, S.J., Bhatt, H.A., Dhamne, A.: Effects of MgO-CaO-P<sub>2</sub>O<sub>5</sub>-Na<sub>2</sub>O-based additives on mechanical and biological properties of hydroxyapatite, *J.Amer.Ceram.Soc.*, **89**, 875-881, (2006).
- 34 Werner, J., Linner-Krömer, B., Friess, W., Greil, P.: Mechanical properties and *in vitro* cell compatibility of hydroxyapatite ceramics with graded pore structure, *Biomaterials*, **23**, 4285-4294, (2002).
- 35 Pompe, W., Worch, H., Epple, M., Friess, W., Gelinsky, M., Greil, P., Hempel, U., Scharnweber, D., Schulte, K.: Functionally graded materials for biomedical applications, *Mat.Sci.Eng. A* **363**, 40-60, (2003).
- 36 Miao, X., Sun, D.: Graded/Gradient Porous Biomaterials, *Materials*, **3**, 26-47, (2010).
- 37 Koh, Y.H., Kim, H.W., Kim, H.E., Halloran, J.W.: Fabrication of Microchannelled-Hydroxyapatite Bioceramic by a Coextrusion Process, *J.Amer.Ceram.Soc.*, **5**, 2578-2580, (2002).
- 38 Arita, I.H., Castano, V.M., Wilkinson, D.S.: Synthesis and Processing of Hydroxyapatite Ceramic Tapes with Controlled Porosity, *J.Mat.Sci.Mat.Med.*, **6**, 19-23, (1995).
- 39 Schindler, K., Roosen, A.: Manufacture of 3D structures by cold low pressure lamination of ceramic green tapes, *J.Europ.Ceram.Soc.*, **29**, 899-904, (2009).
- 40 Soltesz, U., Richter, H., Kienzler, R.: The concentric-ring test and its application for determining the surface strength of ceramics, in *Mater Sci Monogr (Ceram Clin Appl)*, **39**, 149-158, (1987).
- 41 Wang, P.E., Chakl, T.K.: Sintering behaviour and mechanical properties of hydroxylapatite and dicalcium phosphate, *J.Mat.Sci.Mat.Med.*, **4**, 150-158, (1993).
- 42 Nath, S., Biswas, K., Wang, K., Bordia, R.K., Basu, B.: Sintering, Phase Stability and Properties of Calcium Phosphate-Mullite Composites, *J.Amer.Ceram.Soc.*, **93**, 1639-1649, (2010).
- 43 Ramesh, S.: Grain Size-Properties Correlation in Polycrystalline Hydroxyapatite Bioceramic, *Malaysian Journal of Chemistry*, **3**, 35-40, (2001).
- 44 McGeary, R.K.: Mechanical Packing of Spherical Particles, *J.Amer.Ceram.Soc.*, **44**, 513, (1961).
- 45 Funk, J.A., Dinger, D.R.: Predictive Process Control of Crowded Particulate Suspensions, Kluwer Academic Publ., Norwell, MA, (1994).
- 46 Lange, F.F., Lam, D.C.C., Sudre, O.: Powder Processing and Densification of Ceramic Composites, *Mater.Res.Soc.Symp. Proc.*, **155**, 309-318, (1989).
- 47 Rahaman, M.N.: Ceramic Processing, Taylor & Francis, Boca Raton, FL, (2007).
- 48 Bordia, R.K., Raj, R.: Analysis of Sintering of a Composite with a Glass or Ceramic Matrix, *J.Amer.Ceram.Soc.*, **69**, C 55 - C 57, (1986).
- 49 Scherrer, G.W.: Sintering with rigid inclusions, *J.Amer.Ceram.Soc.*, **70**, 719-725, (1987).
- 50 Bordia, R.K., Raj, R.: Sintering Behaviour of Ceramic Films Constrained by a Rigid Substitute, *J.Amer.Ceram.Soc.*, **68**, 287-292, (1985).
- 51 Ruys, A.J., Wei, M., Sorrell, C.C., Dickson, M.R., Brandwood, A., Milthorpe, B.K.: Sintering effects on the strength of hydroxyapatite, *Biomaterials*, **16**, 409-415, (1995).
- 52 Santos, J.D., Knowles, J.C., Reis, R.L., Monteiro, F.J., Hastings, G.W.: Microstructural Characterization of Glass-Reinforced Hydroxyapatite Composites, *Biomaterials*, **15**, 5-10, (1994).
- 53 Giovan, M.N., Sines, G.: Biaxial and Uniaxial Data for Statistical Comparisons of a Ceramic's Strength, *J.Amer.Ceram.Soc.*, **62**, 510-515, (1979).